

Atomic species derived CoO_x clusters on nitrogen doped mesoporous carbon as advanced bifunctional electro-catalysts for Zn-air battery

HPSTAR
1001-2020



Kai Huang^a, Ruyue Wang^{a,b,c}, Shijing Zhao^d, Peng Du^a, Hao Wang^{a,c}, Hehe Wei^b,
Yuanzheng Long^b, Bohan Deng^b, Ming Lei^{a,*}, Binghui Ge^{e,**}, Huiyang Gou^d, Ru Zhang^{a,c},
Hui Wu^{b,***}

^a State Key Laboratory of Information Photonics and Optical Communications, School of Science, Beijing University of Posts and Telecommunications, Beijing, 100876, China

^b State Key Laboratory of New Ceramics and Fine Processing, School of Materials Science and Engineering, Tsinghua University, Beijing, 100084, China

^c Beijing Key Laboratory of Space-ground Interconnection and Convergence, Beijing University of Posts and Telecommunications (BUPT), Xitucheng Road NO.10, Beijing, 100876, China

^d Center for High Pressure Science and Technology Advanced Research, Beijing, 100094, China

^e Key Laboratory of Structure and Functional Regulation of Hybrid Materials, Ministry of Education, Institutes of Physical Science and Information Technology, Anhui University, Hefei, 230601, China

ARTICLE INFO

Keywords:

Solution synthesis
CoO_x clusters
Oxygen electrode
Zn-air battery

ABSTRACT

The development of earth-abundant and cost-effective electro-catalysts at the air cathodes for both oxygen reduction and evolution reactions (ORR and OER) with sluggish kinetics are central to the overall performance of rechargeable metal-air batteries, remaining an issue that is gaining increasing interest in recent years. Herein, we report a nitrogen-doped mesoporous carbon supported clustered CoO_x composite catalyst (CoO_x/NMC) synthesized from the anchored atomically dispersed CoOOH species by an efficient two-step nucleation method. Due to the synergistic and size effects, CoO_x/NMC exhibits an enhanced bifunctional electrocatalytic performance in alkaline media than the state of the art commercial Pt/C catalyst for ORR and the OER catalyst (Ir/C). More importantly, the advanced CoO_x/NMC catalyst enables recharge Zn-air batteries (ZABs) to achieve long-term cycling performance over 400 h by galvanostatic charge-discharge at current density of 10 mA cm⁻² with high efficiency, suggesting a very promising alternative to the conventional Pt/C and Ir/C catalysts for an air cathode.

Rechargeable metal-air batteries, especially Zn-air batteries (ZABs) have been targeted as one of the most promising energy storage systems for future electric vehicles and other next-generation portable devices, because of their high theoretical energy density, low cost, environmental friendliness and improved safety [1–3]. The efficiency of charge-discharge processes of ZABs is significantly restrained by the oxygen electrode electro-catalysis at air cathodes, where the oxygen reduction reaction (ORR) is stimulated by electrons from the current collector and combine with metal dissolved in the electrolyte during discharging, and the reverse oxygen evolution reaction (OER) process occurs during charging [4,5]. However, the multistep and proton-coupled electron transfer processes of the reversible oxygen reactions lead to sluggish kinetics for ORR/OER, which has been the

long-standing bottlenecks of inefficient and unideal lifetime [6,7]. Therefore, the major challenge for ZABs is the development of stable and effective bifunctional electrocatalysts, possibly working in aqueous electrolytes with air as the oxygen source. Although precious-metal-based electrocatalysts (Pt, Ru, Ir, and their alloys) have been used as oxygen electrocatalysts, their insufficient catalytic bifunctionality, high cost, and scarcity still impede the large-scale commercialization of ZABs technology [6–8]. Hence, the development of earth-abundant, low-cost, highly efficient and durable bifunctional electrocatalysts is inevitable for designing advanced rechargeable metal-air batteries [9–11].

Alternatively, various transition-based catalysts with high activity and good durability have been extensively studied, such as transition-

* Corresponding author.

** Corresponding author.

*** Corresponding author.

E-mail addresses: mlei@bupt.edu.cn (M. Lei), bhge@ahu.edu.cn (B. Ge), huiwu@tsinghua.edu.cn (H. Wu).

based metal oxides [12–14], chalcogenides [15], nitrides [16,17], metal-heteroatom doped carbon materials and carbon hybrids [18–20]. Among these catalysts, N-doped carbon materials supported metal oxide (especially CoO_x -based oxides) composite catalysts have attracted considerable attentions, due to their unique 3d electronic configurations and high surface chemical activity as well as the high charge transport capacity of carbon matrix [21,22]. For example, Muhler and co-workers obtained highly active bifunctional electrocatalysts for oxygen electrodes comprising core-shell $\text{Co@Co}_3\text{O}_4$ nanoparticles embedded in CNT-grafted N-doped carbon-polyhedra obtained by the direct pyrolysis of cobalt metal-organic framework (ZIF-67) in a reductive H_2 atmosphere and subsequent controlled oxidative calcination [23]. Chen et al. also developed a hybrid of interpenetrating metallic Co and spinel Co_3O_4 “janus” nanoparticles stitched in porous graphitized shells ($\text{Co/Co}_3\text{O}_4\text{@PGS}$) as an efficient bifunctional electrocatalyst for oxygen reduction and evolution reactions, via an ionic exchange and the following pyrolysis induced redox between Co^{2+} and 2D metal-organic-framework nanosheets [24]. However, conventional synthesis by thermal pyrolysis metal-containing precursor cannot control the chemical state of Co species (uncontrollable size, morphology and structure of active sites), which will severely hinder the electron transfer and reaction processes and thus result in sluggish reaction kinetics and larger polarizations [25]. To solve these problems and yield

high-performance, it is essential to synergistically optimize the catalytic reactivity and electrical conductivity by understanding and controlling the formation of active sites on suitable carbon substrates, which still remains an open question and challenge.

In this study, ultrafine CoO_x clusters (2–3 nm) deriving from atomically dispersed CoOOH species were fabricated on the surface of nitrogen-doped mesoporous carbon (NMC) substrates by developing a novel two-step synthesis, which exhibits superior ORR/OER electrocatalytic performance and enhanced power output capability toward ZABs. The overall oxygen electrode activity can be evaluated by the difference (ΔE) between half-wave potential ($E_{1/2}$, determining the working discharge voltage) of ORR and potential at 10 mA cm^{-2} ($E_{j=10}$, controlling the working charge voltage) for OER. It is found that CoO_x/NMC exhibits a smaller difference values ($\Delta E_1 = 0.592 \text{ V}$) compared with Pt/C and Ir/C coupled catalysts ($\Delta E_2 = 0.693 \text{ V}$), indicating a superior bifunctionality of CoO_x/NMC composites as advanced electrode catalysts. Moreover, ZABs assembled with CoO_x/NMC air-cathode catalysts also present excellent battery performance with a high open-circuit voltage about 1.48 V and peak power density of 195.3 mW cm^{-2} , which outperforms that of Pt/C + Ir/C and other recently reported nonprecious metals-based catalysts.

As schematic shown in Fig. 1a, the two-step synthetic route for CoO_x/NMC includes the nucleation-inhibited solution synthesis at -40°C and succeeding annealing process at 500°C in argon atmosphere, the

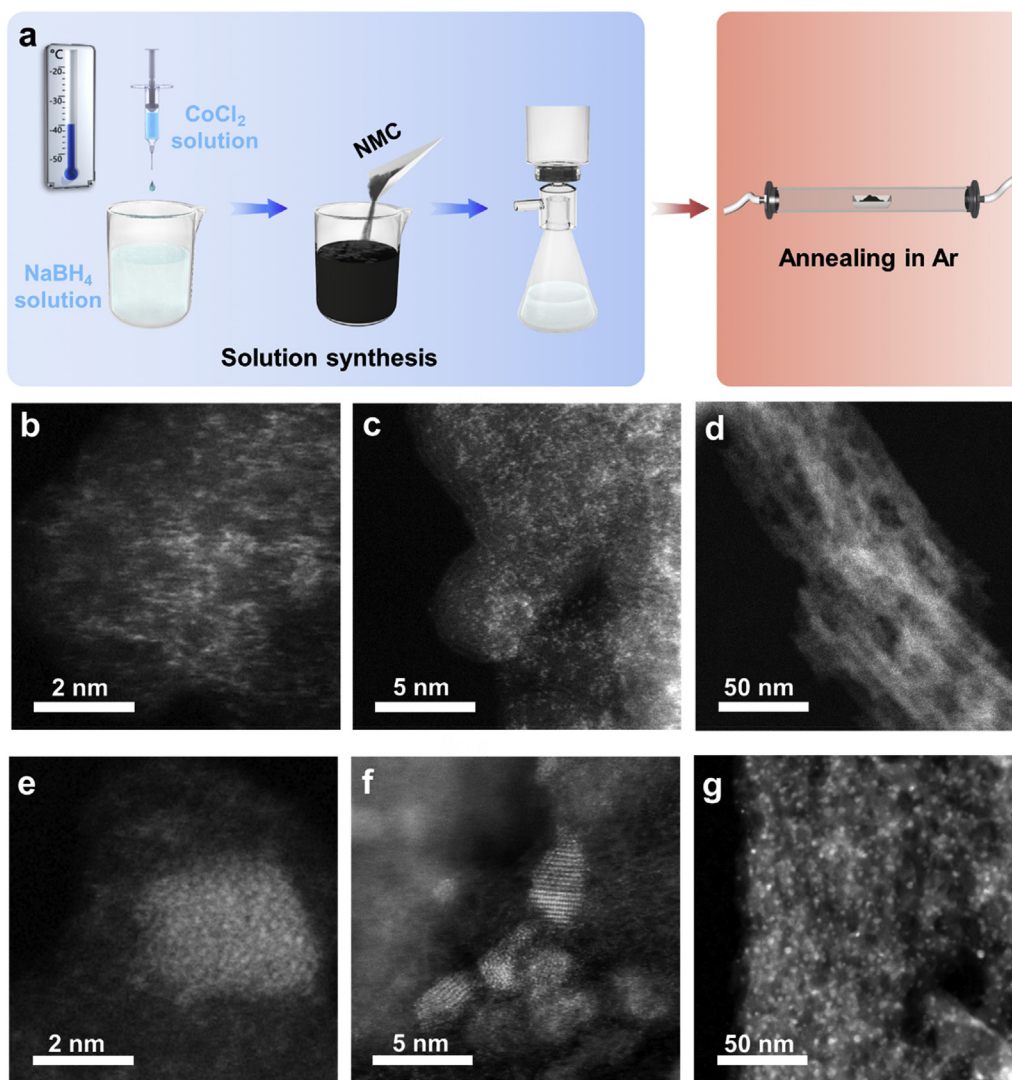


Fig. 1. Materials design and morphology characterization: (a) Schematic illustration for the fabrication of CoO_x/NMC composites. HAADF-STEM images at different magnifications of (b–d) CoOOH/NMC with supported atomically dispersed species and (e–g) CoO_x/NMC with supported ultrafine clusters (2–3 nm).

final cobalt elements content confirmed by ICP-MS measurement is as high as 11.51% (see details in the experimental section). The former solution synthesis yields atomically dispersed species on NMC substrates (CoOOH/NMC) by effectively suppressing nucleation formation, as demonstrated by our previous works via both thermodynamic and kinetic control. In this synthesis route, borohydride (BH_4^-) ions are employed to achieve the sustained release of hydroxyl ion (OH^-) by controlling their self-hydrolysis reaction at -40°C , where the hydride ions H^- are firstly transferred from chemisorbed BH_4^- ions to unoccupied adjacent cobalt metal atoms, then react with the water molecules to produce H_2 and OH^- ions [26]. The aberration-corrected high-angle annular dark field-scanning transmission electron microscopy (HAADF-STEM) of CoOOH/NMC intermediate at different magnifications (Fig. 1b–d), confirm that only atomically dispersed species anchored onto NMC substrates from solution synthesis. After a mild thermal annealing at 500°C for 1 h with a heating rate of 1°C min^{-1} under flowing Ar, STEM images (Fig. 1e–g and Fig. S1), particle size distribution (Fig. S2) and elemental mappings (Fig. S3) all demonstrate the formation of uniform and partially crystalline clusters with sized of

2.54 ± 0.48 nm on NMC surface (CoO_x/NMC), which matches well with our schematic illustration and design. As shown in Fig. S4a, there are no obvious diffraction patterns corresponding to cobalt oxides can be observed in the selected area electron diffraction (SEAD) image, suggesting that no large nanocrystals exist in CoO_x/NMC sample. The element species confirmed by EDS in Fig. S4b can be attributed to C, N, O and Co, consistent with the mapping result of CoO_x/NMC and demonstrating the high purity of CoO_x/NMC . In sharp contrast, a nanosheet-like sample assembled from nanoparticles can be obtained by a controlled room-temperature solution synthesis followed by thermal annealing route. (Fig. S5), which also indicates the significant influence of low-temperature solution reaction (i.e. the initial inhibition of nuclei formation). The annealing temperature also affects the nucleation process, the atomically dispersed CoOOH species on NMC substrate from solution synthesis will dynamically aggregate into larger nanoparticles when the annealing temperature is raised to 750°C ($\text{CoO}_x/\text{NMC-750}$) and 900°C ($\text{CoO}_x/\text{NMC-900}$) as shown in Fig. S6.

To further identify the chemical states and coordination environment of as-prepared samples, characterizations including X-ray diffraction

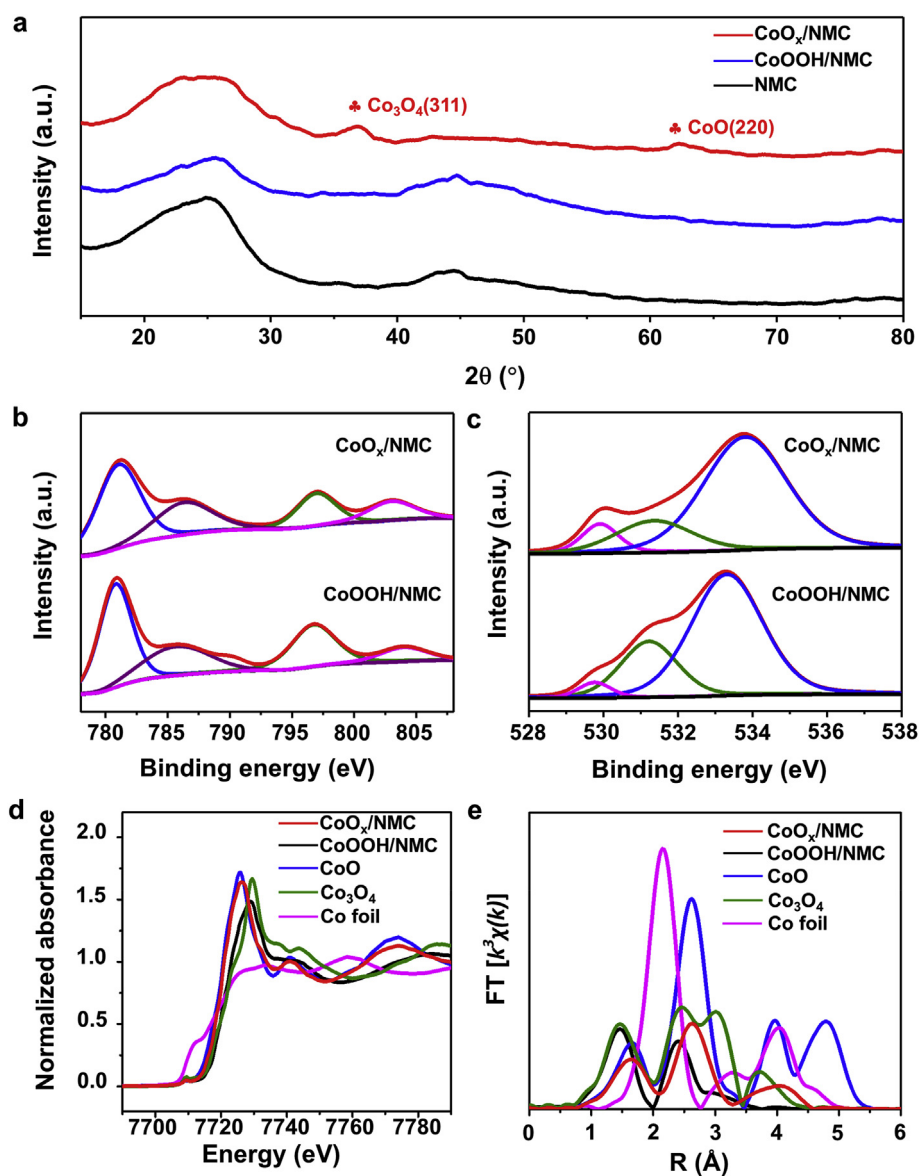


Fig. 2. Structure and composition characterizations: (a) XRD patterns of CoO_x/NMC , CoOOH/NMC and pure NMC substrate. High-resolution XPS spectra of (b) Co 2p and (c) O 1s for CoO_x/NMC , CoOOH/NMC . (d) Normalized X-ray absorption near edge structure (XANES) spectra at Co K-edge and (e) Extended X-ray absorption fine structure (EXAFS) spectra for the Co foil, Co_3O_4 , CoO, CoOOH/NMC and CoO_x/NMC .

(XRD), X-ray photoelectron spectroscopy (XPS) and X-ray absorption fine structure (XAFS) were performed. As displayed in Fig. 2a, two additional Co_3O_4 (311) and CoO (220) peaks can be indexed for CoO_x/NMC sample, while CoOOH/NMC intermediate exhibits no obvious cobalt-based peaks and is almost identical to the pristine NMC substrates. However, Fig. S7 demonstrates that the formation of NaBO_2 impurity without the inhibition of NaBH_4 hydrolysis at room temperature. This result suggests that the uncontaminated clusters will form from atomically dispersed species synthesized at -40°C during thermal annealing process. And there is no B element in the final CoO_x/NMC sample by further rinsing with plenty of ultrapure water before and after annealing as shown in Fig. S8, which is identical with results of EDS elemental mapping and spectrum. Analogously, Fig. 2b displays the high-resolution Co 2p XPS spectra of CoOOH/NMC and CoO_x/NMC samples with a mixed cobalt element valence states of $\text{Co}^{2+}/\text{Co}^{3+}$, where the two non-satellite peaks at 780.7 and 796.5 eV are typical characteristic of CoO and Co_3O_4 respectively [27,28]. The deconvoluted O 1s spectra exhibit three peaks at 529.7, 531.3 and 533.3 eV, ascribing to the surface lattice oxygen (O_L), surface adsorbed hydroxyl groups (O_{OH}) and chemisorbed water (O_{MW}), respectively [29]. Obviously, the O_L component in CoO_x/NMC increases compared with CoOOH/NMC , which also indicating a thermal transformation from CoOOH to CoO_x . In addition, a majority of pyridinic-N and graphitic-N (centered at the binding energies of 400.8 and 398.5 eV, respectively) can serve as effective binding to enhance interactions between supports and metal atoms (Fig. S10) [30,31].

X-ray absorption fine structure (XAFS) spectroscopy is performed to

understand the oxidation state and coordination environments of Co-containing compounds (as shown in Fig. 2d and e). A small peak appears on the pre-edge of CoO_x/NMC in comparisons with standard CoO and its intensity is weaker than that of Co_3O_4 (as shown in Fig. S11). Different from highly symmetrical Co–O octahedron in CoO , this pre-edge is mainly attributed to dipolar forbidden transition $1s$ to $3d$ characteristic of the tetrahedrally coordinated Co^{2+} [32], due to that the tetrahedral ligand field allows a dipolar transition, while only a quadrupolar transition is allowed for $1s$ to $3d$ in the octahedral symmetry [33]. This fact also supports the trace of Co_3O_4 presented in CoO_x/NMC . Moreover, the white-line profile of CoO_x/NMC resembles that of CoO standard but differs from CoOOH/NMC , Co_3O_4 and Co foil, and the absorption edge of CoO_x/NMC locate between those of CoO and Co_3O_4 , supporting the possible coexistence of CoO and Co_3O_4 phase as revealed by XRD and XPS results. Fig. 2e shows the coordination environment of the Co atom evaluated by Fourier transformed (FT) using k^3 -weighted extended X-ray absorption fine structure (EXAFS) spectra of Co K-edge. Notably, CoO_x/NMC sample exhibits two dominant peaks at 1.65 and 2.63 Å in R space, which are assigned to the nearest Co–O and Co–Co coordination, respectively. Both of two peaks are weaker than that of standard CoO , especially for the second peak. From EXAFS analysis in Fig. S12a and Tables S1 and S3, the coordination numbers of O and Co atoms are found to be 3.99 and 5.63, much lower than theoretical values of CoO (6 and 12), suggesting the presence of abundant defects to boost the catalytic properties [34]. The absorption edge of CoOOH/NMC is similar to Co_3O_4 , indicating the close average valence state of cobalt in

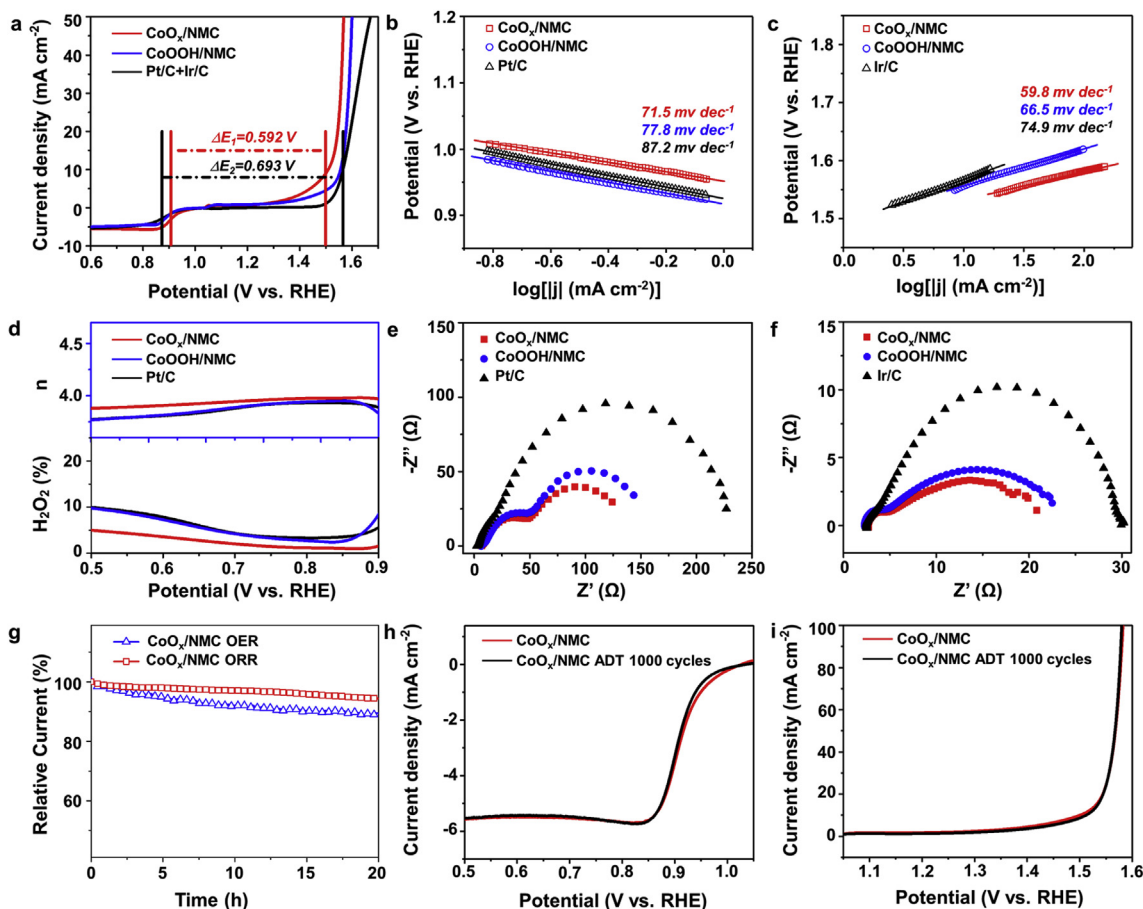


Fig. 3. Oxygen electrode catalytic performance of different catalysts in 1 M KOH: (a) Bifunctional ORR/OER polarization curves of CoO_x/NMC , CoOOH/NMC and commercial Pt/C and Ir/C catalysts. Tafel plots of (b) the corresponding ORR polarizations curves and (c) the corresponding OER polarizations curves. (d) Electron transfer number n (top) and H_2O_2 yield (bottom) vs. potential. Nyquist plots obtained from EIS measurements at (e) 0.85 V (vs. RHE) in N_2 -saturated electrolyte and (f) 1.55 V (vs. RHE) in O_2 -saturated electrolyte. (g) Chronoamperometry (CA) curves of CoO_x/NMC at 1.49 V for OER and 0.90 V vs. RHE for ORR. Stability tests by ADT method for CoO_x/NMC under (h) ORR and (i) OER conditions, where polarization curves are collected before and after 1000 CV cycles.

these two materials, which is also confirmed by good fitting of FT curve using both CoOOH and Co, rather than CoOOH itself (Figs. S12b and S9c, Table S2). Therefore, the presence of both CoOOH and Co leads to the decreasing valence states compared with CoOOH, agreeing well with XPS results. Furthermore, we also perform a linear fitting of relationship between valence state and E_0 (the energy value of 0.5 of normalized spectra) [35], where the average valences of CoO_x/NMC and CoOOH@NMC are found to be ~2.28 and 2.61, respectively (as shown in

Fig. S13), consistent with the analyses of change of pre-edge peak and Fourier transformed EXAFS, as well as curves-fitting results.

Fig. 3a shows the overall oxygen electrode polarization curves of CoO_x/NMC, CoOOH/NMC and commercial Pt/C coupled with Ir/C catalysts in 1 M KOH solution, confirming the enhanced ORR and OER activities of CoO_x/NMC. The bifunctionality indicator (ΔE) between the ORR half-wave potential ($E_{1/2}$) and potential at the OER current density of 10 mA cm⁻² ($E_{j=10}$) for CoO_x/NMC catalyst is 0.592 V, much smaller

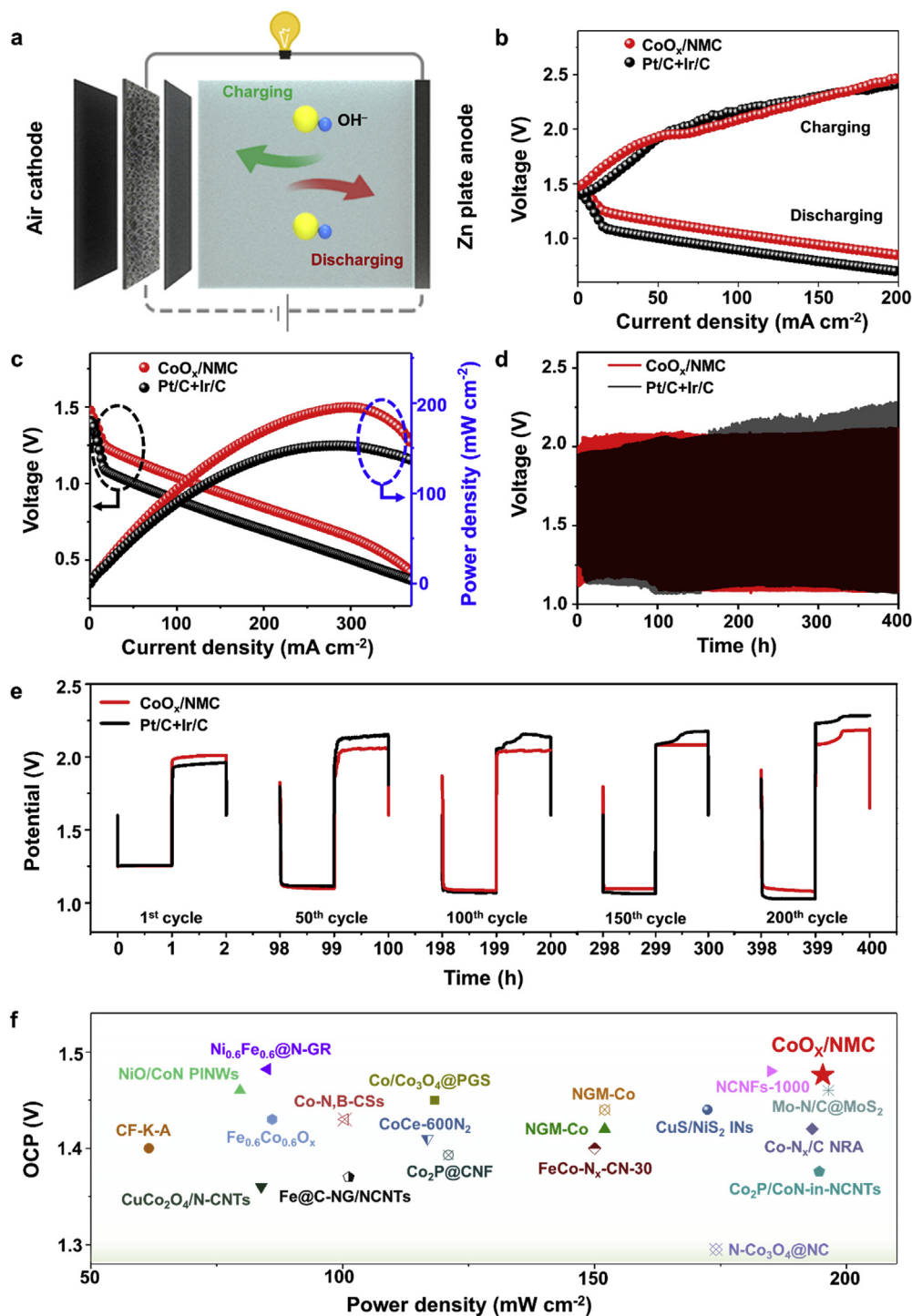


Fig. 4. Rechargeable Zn-air battery performance with different catalysts: (a) Schematic illustration for the charge and discharge process. (b) Charge and discharge polarization curves. (c) Power density and polarization plots. (d) Battery cycling test at charging and discharging current densities of 10 mA cm⁻² (2 h per cycle). (e) Detailed comparison between CoO_x/NMC and other state-of-the-art ORR/OER catalysts for cathodes, in view of open circuit potential (OCP) and power density.

than that of CoOOH/NMC (0.658 V) and Pt/C + Ir/C (0.693 V) catalysts, respectively. As shown in Figs. S14–15, the degradation of oxygen electrode catalytic activity for CoO_x/NMC, compared with other controlled samples at different annealing temperatures, indicates the significant influence of regulating nuclei formation. The excellent oxygen electrode catalytic activity of CoO_x/NMC catalysts is further evidenced by reaction kinetics with the lowest Tafel slopes of 71.5 and 59.8 mV dec⁻¹ (Fig. 3b–c and Fig. S14), respectively. The high selectivity of CoO_x/NMC toward a dominated 4 e⁻ charge transfer has also been confirmed for ORR in Fig. 3d. Table S7 also summarizes that CoO_x/NMC exhibits a surpassed bifunctional oxygen electrocatalytic activity with respect to recently reported various cobalt oxides nanocatalysts. To illuminate the enhanced oxygen-electrode activity of CoO_x/NMC catalyst, the Nyquist plots obtained from electrochemical impedance spectroscopy (EIS) measurements have been provided. As shown in Fig. 3e and f and Table S8, CoO_x/NMC based electrodes exhibit the smallest charge-transfer resistance (R_{ct1}) for both ORR and OER, suggesting an enhanced electrochemical reaction process. Moreover, the electrochemical durability and stability are other critical criteria in evaluating the performance of the electrocatalysts in practical applications. Fig. 3g shows that CoO_x/NMC catalysts can maintain the vast majority of ORR and OER activities (more than 90% of initial current densities) for a 20 h long-termed chronoamperometry (CA) test. In addition, the continuous cyclic voltammetry (CV) scanning within the potential ranges of 0.57–1.07 V (vs. RHE) for ORR and 1.02–1.72 V (vs. RHE) for OER at 100 mV s⁻¹ in Fig. 3h and i, also demonstrate that CoO_x/NMC catalysts almost maintain an unchanged catalytic activity with negligible decay in current density in comparisons with CoOOH/NMC and Pt/C + Ir/C catalysts (Fig. S16). These results confirm that the ultrafine CoO_x clusters loading can effectively promote the ORR and OER performance under alkaline conditions.

Stimulated by the promising bifunctional activity discussed above, a rechargeable Zn-air battery was fabricated with CoO_x/NMC catalyst as the air cathode as illustrated in Fig. 4a and Fig. S17. A mixture of state-of-the-art commercial Pt/C and Ir/C with equal ratios was also tested in Zn-air battery as the reference. The results show that CoO_x@NMC-based battery delivers an open-circuit voltage as high as 1.48 V, a much smaller charge-discharge voltage gap especially at relatively high current densities (Fig. 4b) and a higher peak power density of 195.3 mW cm⁻² (Fig. 4c) than Pt/C + Ir/C based battery and most recently reported works [5,24,36–52], demonstrating the optimized performance of CoO_x/NMC catalysts. Fig. S18 displays the galvanostatic discharge curves recorded at the discharge current density of 10 mA cm⁻² with a voltage plateau of 1.17 V, and the calculated corresponding energy density, relative to the normalized amount of zinc electrode consumed, is about 849.6 mWh g⁻¹. The high power and energy densities can be attributed to the efficient charge transfer ability and improved accessibility of electrolyte as well as oxygen species of CoO_x@NMC, serving as the non-precious catalyst for Zn-air batteries. Moreover, the long-term rechargeability for the air electrode as one of the most important factors is evaluated by galvanostatic charge-discharge at a current density of 10 mA cm⁻² with each cycle 2 h for 200 cycles. As illustrated in Fig. 4d and e, CoO_x/NMC based ZABs provides a similar charge-discharge gap to the noble-metal reference at initial dozens of cycles and maintain the steady and lower voltage gap over 400 h, compared with the obviously increased charge-discharge gap of noble metal-based Zn-air batteries. As discussed above, the ZABs with CoO_x/NMC catalysts exhibit a superior charge-discharge capacity and stability due to their excellent bifunctional ORR/OER electrocatalytic activity and stability, which outperforms most of other recently reported low-cost bifunctional oxygen electrocatalysts (Fig. 4f and Table S9).

In summary, we have demonstrated a highly efficient CoO_x/NMC bifunctional catalyst for a rechargeable Zn-air battery application by a novel strategy, combining an ultralow temperature solution synthesis with salt-assisted annealing. It is found that ultrafine CoO_x cluster (sizes of 2.54 ± 0.48 nm) can be directly derived from supported atomically dispersed CoOOH moieties, yielded from the sustained release of

hydroxyl ion (OH⁻) from the self-hydrolysis of borohydride (BH₄⁻) ions at -40 °C. Benefiting from the superior ORR and OER catalytic activities and stabilities than Pt/C and Ir/C catalysts confirmed by the enhanced Tafel kinetic and charge transfer, CoO_x/NMC catalyst enables recharge Zn-air batteries (ZABs) to achieve long-term cycling performance over 400 h at a current density of 10 mA cm⁻² with high efficiency in alkaline media. Considering the versatility of atomic scale regulation, this study will further promote the rational design of efficient hybrid electrocatalysts for diverse applications in renewable energy storage and conversion.

Declaration of competing interest

The authors declare that they have no known competing financial interests or personal relationships that could have appeared to influence the work reported in this paper.

CRediT authorship contribution statement

Kai Huang: Conceptualization, Data curation, Formal analysis, Funding acquisition, Project administration, Writing - original draft, Writing - review & editing. **Ruyue Wang:** Data curation, Investigation, Methodology, Validation, Writing - original draft, Writing - review & editing. **Shijing Zhao:** Formal analysis, Writing - original draft. **Peng Du:** Methodology, Writing - original draft. **Hao Wang:** Formal analysis, Methodology. **Hehe Wei:** Methodology, Visualization. **Yuanzheng Long:** Investigation, Methodology. **Bohan Deng:** Investigation, Methodology. **Ming Lei:** Funding acquisition, Resources, Writing - review & editing. **Binghui Ge:** Resources, Visualization, Writing - review & editing. **Huiyang Gou:** Formal analysis, Writing - original draft. **Ru Zhang:** Formal analysis, Writing - original draft. **Hui Wu:** Funding acquisition, Resources, Writing - original draft, Writing - review & editing.

Acknowledgements

We acknowledge the financial support from the National Natural Science Foundation of China of China (Grant Nos. 51902027, 51788104, 51661135025, 51706117, and U1564205), National Basic Research of China (Grants Nos. 2015CB932500, 2016YFE0102200 and 2018YFB0104404), Fundamental Research Funds for the Central Universities (Grant Nos. 2019RC20) and Fund of State Key Laboratory of Information Photonics and Optical Communications (Beijing University of Posts and Telecommunications, P.R. China). We also thank the XAFS station (BL14W1) of the Shanghai Synchrotron Radiation Facility.

Appendix A. Supplementary data

Detailed experimental procedures, supporting figures are available in the supplementary information.

Supplementary data to this article can be found online at <https://doi.org/10.1016/j.ensm.2020.03.026>.

References

- [1] J. Zhang, Z. Zhao, Z. Xia, et al., A metal-free bifunctional electrocatalyst for oxygen reduction and oxygen evolution reactions, *Nat. Nanotechnol.* 444 (2015) 10.
- [2] J. Fu, Z.P. Cano, M.G. Park, et al., Electrically rechargeable zinc-air batteries: progress, challenges, and perspectives, *Adv. Mater.* 29 (2017) 1604685.
- [3] F. Meng, H. Zhong, D. Bao, et al., In situ coupling of strung Co₄N and intertwined N-C fibers toward free-standing bifunctional cathode for robust, efficient, and flexible Zn-air batteries, *J. Am. Chem. Soc.* 138 (2016) 10226.
- [4] J. Park, M. Risch, G. Nam, et al., Single crystalline pyrochlore nanoparticles with metallic conduction as efficient bi-functional oxygen electrocatalysts for Zn-air batteries, *Energy Environ. Sci.* 10 (2017) 129.
- [5] J. Yin, Y. Li, F. Lv, et al., NiO/CoN porous nanowires as efficient bifunctional catalysts for Zn-air batteries, *ACS Nano* 11 (2017) 2275.
- [6] H.F. Wang, Q. Xu, Materials design for rechargeable metal-air batteries, *Matter* 1 (2019) 565–595.

- [7] J. Pan, Y.Y. Xu, H. Yang, et al., Advanced architectures and relatives of air electrodes in Zn-air batteries, *Adv. Sci.* 5 (2018) 1700691.
- [8] Y. Li, M. Gong, Y. Liang, et al., Advanced zinc-air batteries based on high-performance hybrid electrocatalysts, *Nat. Commun.* 4 (2013) 1805.
- [9] J.S. Lee, S.T. Kim, R. Cao, et al., Metal-air batteries with high energy density: Li-air versus Zn-air, *Adv. Energy Mater.* 1 (2011) 34.
- [10] E. Davari, D.G. Ivey, Bifunctional electrocatalysts for Zn-air batteries, *Sustain. Energy Fuels* 2 (2018) 39.
- [11] Z.F. Huang, J. Wang, Y. Peng, et al., Design of efficient bifunctional oxygen reduction/evolution electrocatalyst: recent advances and perspectives, *Adv. Energy Mater.* 7 (2017) 1700544.
- [12] Y. Liu, C. Xiao, M. Lyu, et al., Ultrathin Co_3S_4 nanosheets that synergistically engineer spin states and exposed polyhedra that promote water oxidation under neutral conditions, *Angew. Chem. Int. Ed.* 127 (2015) 11383.
- [13] O. Mabayoje, A. Shoola, B.R. Wygant, et al., The role of anions in metal chalcogenide oxygen evolution catalysis: electrodeposited thin films of nickel sulfide as “pre-catalysts”, *ACS Energy Lett* 1 (2016) 195.
- [14] H.F. Wang, C. Tang, B. Wang, et al., Bifunctional transition metal hydroxysulfides: room-temperature sulfurization and their applications in Zn-air batteries, *Adv. Mater.* 29 (2017) 1702327.
- [15] J. Sun, H. Yin, P. Liu, et al., Molecular engineering of Ni-/Co-porphyrin multilayers on reduced graphene oxide sheets as bifunctional catalysts for oxygen evolution and oxygen reduction reactions, *Chem. Sci.* 7 (2016) 5640.
- [16] Z. Cui, G. Fu, Y. Li, J.B. Goodenough, Ni_3FeN -supported Fe_3Pt intermetallic nanoalloy as a high-performance bifunctional catalyst for metal-air batteries, *Angew. Chem. Int. Ed.* 56 (2017) 9901.
- [17] K.R. Yoon, K. Shin, J. Park, et al., Brush-like cobalt nitride anchored carbon nanofiber membrane: current collector-catalyst integrated cathode for long cycle Li-O_2 batteries, *ACS Nano* 12 (2018) 128.
- [18] J. Zhang, Z. Zhao, Z. Xia, L. Dai, A metal-free bifunctional electrocatalyst for oxygen reduction and oxygen evolution reactions, *Nat. Nanotechnol.* 10 (2015) 444.
- [19] K. Sakaushi, T.P. Fellinger, M. Antonietti, Bifunctional metal-free catalysis of mesoporous noble carbons for oxygen reduction and evolution reactions, *ChemSusChem* 8 (2015) 1156.
- [20] H.B. Yang, J. Miao, S.F. Hung, et al., Identification of catalytic sites for oxygen reduction and oxygen evolution in N-doped graphene materials: development of highly efficient metal-free bifunctional electrocatalyst, *Sci. Adv.* 2 (2016), e1501122.
- [21] J. Meng, C. Niu, L. Xu, et al., General oriented formation of carbon nanotubes from metal-organic frameworks, *J. Am. Chem. Soc.* 139 (2017) 8212.
- [22] J. Xiao, Y. Xia, C. Hu, et al., Raisin bread-like iron sulfides/nitrogen and sulfur dual-doped mesoporous graphitic carbon spheres: a promising electrocatalyst for the oxygen reduction reaction in alkaline and acidic media, *J. Mater. Chem. A* 5 (2017) 11114.
- [23] A. Aijaz, J. Masa, M.S.C. Rösler, et al., $\text{Co}@\text{Co}_3\text{O}_4$ encapsulated in carbon nanotube-grafted nitrogen-doped carbon polyhedra as an advanced bifunctional oxygen electrode, *Angew. Chem. Int. Ed.* 55 (2016) 4087.
- [24] Y. Jiang, Y.P. Deng, J. Fu, et al., Interpenetrating triphase cobalt-based nanocomposites as efficient bifunctional oxygen electrocatalysts for long-lasting rechargeable Zn-air batteries, *Adv. Energy Mater.* 8 (2018) 1702900.
- [25] M. Yu, Z. Wang, C. Hou, et al., Nitrogen-doped Co_3O_4 mesoporous nanowire arrays as an additive-free air-cathode for flexible solid-state zinc-air batteries, *Adv. Mater.* 29 (2017) 1602868.
- [26] R. Fernandes, N. Patel, A. Miotello, et al., Studies on catalytic behavior of Co-Ni-B in hydrogen production by hydrolysis of NaBH_4 , *J. Mol. Catal. Chem.* 298 (2009) 1–6.
- [27] W. Xu, F. Lyu, Y. Bai, et al., Porous cobalt oxide nanoplates enriched with oxygen vacancies for oxygen evolution reaction, *Nano Energy* 43 (2018) 110–116.
- [28] F. Xie, R. Xie, J.X. Zhang, et al., Direct reductive quinolyl β -C-H alkylation by multispherical cavity carbon-supported cobalt oxide nanocatalysts, *ACS Catal.* 7 (2017) 4780–4785.
- [29] C. Weerakkody, S. Biswas, W. Song, et al., Controllable synthesis of mesoporous cobalt oxide for peroxide free catalytic epoxidation of alkenes under aerobic conditions, *Appl. Catal. B Environ.* 221 (2018) 681–690.
- [30] K. Huang, L. Zhang, T. Xu, et al., 60 °C solution synthesis of atomically dispersed cobalt electrocatalyst with superior performance, *Nat. Commun.* 10 (2019) 606.
- [31] K. Huang, R. Wang, H. Wu, et al., Direct immobilization of an atomically dispersed Pt catalyst by suppressing heterogeneous nucleation at -40 °C, *J. Mater. Chem. A* 7 (2019) 25779–25784.
- [32] J.H. Choy, H. Jung, J.B. Yoon, Co K-edge XAS study on a new cobalt-doped SiO_2 pillared clay, *Synchrotron Radiat* 8 (2001) 599–601.
- [33] V.R. Elías, N.I. Cuello, L. Andriani, et al., Advances in the study of nano-structured Co/MCM-41 materials: surface and magnetic characterization, *J. Porous Mater.* 25 (2018) 789–799.
- [34] S. Cao, F. Tao, Y. Tang, et al., Size- and shape-dependent catalytic performances of oxidation and reduction reactions on nanocatalysts, Li, J. Yu, *Chem. Soc. Rev.* 45 (2016) 4747.
- [35] H. Dau, P. Liebisch, M. Haumann, X-ray absorption spectroscopy to analyze nuclear geometry and electronic structure of biological metal centers-potential and questions examined with special focus on the tetra-nuclear manganese complex of oxygenic photosynthesis, *Anal. Bioanal. Chem.* 376 (5) (2003) 562–583.
- [36] L. An, Y. Li, M. Luo, et al., Atomic-level coupled interfaces and lattice distortion on CuS/NiS_2 nanocrystals boost oxygen catalysis for flexible Zn-air batteries, *Adv. Funct. Mater.* 27 (2017) 1703779.
- [37] B. Chen, X. He, F. Yin, et al., MO-Co@N-doped carbon (M = Zn or Co): vital roles of inactive Zn and highly efficient activity toward oxygen reduction/evolution reactions for rechargeable Zn-air battery, *Adv. Funct. Mater.* (2017) 1700795.
- [38] H. Cheng, M.L. Li, C.Y. Su, et al., Cu-Co bimetallic oxide quantum dot decorated nitrogen-doped carbon nanotubes: a high-efficiency bifunctional oxygen electrode for Zn-air batteries, *Adv. Funct. Mater.* (2017) 1701833.
- [39] I.S. Amiin, X. Liu, Z. Pu, et al., From 3D ZIF nanocrystals to Co-N_x/C nanorod array electrocatalysts for ORR, OER, and Zn-air batteries, *Adv. Funct. Mater.* (2017) 1704638.
- [40] P. Liu, D. Gao, W. Xiao, et al., Self-powered water-splitting devices by core-shell NiFe@N-graphite-based Zn-air batteries, *Adv. Funct. Mater.* (2018) 1706928.
- [41] Q. Liu, Y. Wang, L. Dai, et al., Scalable fabrication of nanoporous carbon fiber films as bifunctional catalytic electrodes for flexible Zn-air batteries, *Adv. Mater.* 28 (2016) 3000–3006.
- [42] L. Wei, H.E. Karahan, S. Zhai, et al., Amorphous bimetallic oxide-graphene hybrids as bifunctional oxygen electrocatalysts for rechargeable Zn-air batteries, *Adv. Mater.* (2017) 1701410.
- [43] C. Tang, B. Wang, H.F. Wang, et al., Defect engineering toward atomic Co-N_x-C in hierarchical graphene for rechargeable flexible solid Zn-air batterie, *Adv. Mater.* (2017) 1703185.
- [44] Y. Guo, P. Yuan, J. Zhang, et al., $\text{Co}_2\text{P-CoN}$ double active centers confined in N-doped carbon nanotube: heterostructural engineering for trifunctional catalysis toward HER, ORR, OER, and Zn-air batteries driven water splitting, *Adv. Funct. Mater.* (2018) 1805641.
- [45] Z. Wang, W. Xu, X. Chen, et al., Defect-rich nitrogen doped $\text{Co}_3\text{O}_4/\text{C}$ porous nanocubes enable high-efficiency bifunctional oxygen electrocatalysis, *Adv. Funct. Mater.* (2019) 1902875.
- [46] J. Gao, J. Wang, L. Zhou, et al., $\text{Co}_2\text{P}@N$, P-codoped carbon nanofiber as free-standing air electrode for Zn-air batteries: synergy effects of CoN_x satellites shells, *ACS Appl. Mater. Interfaces* 11 (10) (2019) 10364–10372.
- [47] Y. Guo, P. Yuan, J. Zhang, et al., Carbon nanosheets containing discrete Co-N_x-B_y-C active sites for efficient oxygen electrocatalysis and rechargeable Zn-air batteries, *ACS Nano* 12 (2) (2018) 1894–1901.
- [48] I.S. Amiin, Z. Pu, X. Liu, et al., Multifunctional Mo-N/C@MoS₂ electrocatalysts for HER, OER, ORR, and Zn-air batteries, *Adv. Funct. Mater.* (2017) 1702300.
- [49] S. Li, C. Cheng, X. Zhao, et al., Active salt/silica-templated 2D mesoporous FeCo-N_x-carbon as bi-functional oxygen-electrodes for Zn-air batteries, *Angew. Chem. Int. Ed.* 57 (2018) 1856.
- [50] Q. Wang, Y. Lei, Z. Chen, et al., Fe/Fe₃C@C nanoparticles encapsulated in N-doped graphene-CNTs framework as an efficient bifunctional oxygen electrocatalyst for robust rechargeable Zn-air batteries, *J. Mater. Chem. A* 6 (2018) 516–526.
- [51] X. He, X. Yi, F. Yin, et al., Less Active CeO₂ regulating bifunctional oxygen electrocatalytic activity of $\text{Co}_3\text{O}_4@N$ -doped carbon for Zn-air battery, *J. Mater. Chem. A* 7 (2019) 6753–6765.
- [52] H. Jiang, Y. Liu, W. Li, et al., Co nanoparticles confined in 3D nitrogen-doped porous carbon foams as bifunctional electrocatalysts for long-life rechargeable Zn-air batteries, *Small* 14 (2018) 1703739.